Journal of Pressure Vessel Technology, 121(3):315-322, 1999.
(Preprint - see journal for final version http://dx.doi.org/10.1115/1.2883709).

The structural response of cylindrical shells to internal shock loading

W.M. Beltman
University of Twente
Faculty of Mechanical Engineering
P.O. Box 217
7500 AE Enschede
The Netherlands

E.N. Burcsu
California Institute of Technology
Graduate Aeronautical Laboratories
Pasadena
CA 91125
U.S.A.

J.E. Shepherd
California Institute of Technology
Graduate Aeronautical Laboratories
Pasadena
CA 91125
U.S.A.

L. Zuhal
California Institute of Technology
Graduate Aeronautical Laboratories
Pasadena
CA 91125
U.S.A.

Abstract

The internal shock loading of cylindrical shells can be represented as a step load advancing at constant speed. Several analytical models are available to calculate the structural response of shells to this type of loading. These models show that the speed of the shock wave is an important parameter. In fact, for a linear model of a shell of infinite length, the amplitude of the radial deflection becomes unbounded when the speed of the shock wave is equal to a critical velocity. It is evident that simple (static) design formulas are no longer accurate in this case. The present paper deals with a numerical and experimental study on the structural response of a thin aluminum cylindrical shell to shock loading. Transient finite element calculations were carried out for a range of shock speeds. The results were compared to experimental results obtained with the GALCIT 6-inch shock tube facility. Both the experimental and the numerical results show an increase in amplitude near the critical velocity, as predicted by simple steady state models for shells of infinite length. However, the finite length of the shell results in some transient phenomena. These phenomena are related to the reflection of structural waves and the development of the deflection profile when the shock wave enters the shell.

Nomenclature

E	Young's modulus	N/m^2
G	shear modulus	N/m^2
N_{xx}	axial stress resultant	N/m
$N_{\theta\theta}$	circumferential stress resultant	N/m
M_{xx}	moment resultant	N
Q_x	shear stress resultant	N/m
R	shell mean radius	m
f	frequency	Hz
h	shell thickness	m
i	imaginary unit	
k	wave number	$1/m$
l	shell length	m
m, m_1, m_2	characteristic roots	
n	characteristic root	
p_1	pre-shock pressure	Pa
p_2	post-shock pressure	Pa
p_{atm}	atmospheric pressure	Pa
t	time	s
u	axial deflection	m
$\overline{u}$	dimensionless axial deflection	
v	shock speed	m/s
v_d	dilatational wave speed	m/s
v_s	shear wave speed	m/s
w	radial deflection	m
$\overline{w}$	dimensionless radial deflection	
$\overline{w}_b$	dimensionless radial deflection, bending	
$\overline{w}_b^I$	dimensionless radial deflection region I	
$\overline{w}_b^{II}$	dimensionless radial deflection region II	
x	axial coordinate	m
α	characteristic root	
β	shell thickness parameter	
$\overline{\eta}$	dimensionless (moving) axial coordinate	

Δp	pressure difference across shell	Pa
κ	shear correction factor	
ν	Poisson's ratio	
ρ	density	kg/m^3
ψ	rotation	
$\overline{\psi}$	rotation	
Λ_j	excitation parameter (j=1,2)	
Λ_j^s	excitation parameter (j=1,2)	

1 Introduction

This study is concerned with measuring and predicting the deformations of cylindrical shells due to internal shock loading. The load is characterized by a step in pressure or shock wave, pre- and post-shock pressures p_1 and p_2, propagating axially with speed v in the gas within the shell. The moving load excites flexural waves in the shell and produces a net radial deformation due to the difference in pressure across the shock wave. A schematic of the configuration is shown in Fig. 1; the deformations of the tube have been exaggerated to emphasize the type of shell motion we are considering. The most interesting aspect of this problem is that the circumferential strain can greatly exceed (up to 3 to 4 times higher) the equivalent static strain if the shock and flexural motions are in resonance. The present study addresses the linear-elastic regime so that although we consider large strains, they are not so high that plastic deformation or disturbance to the gas flow results. The resonance of the shock in the gas with the flexural waves in the shell are a dynamic effect, which we have studied with transient analyses and experiments.

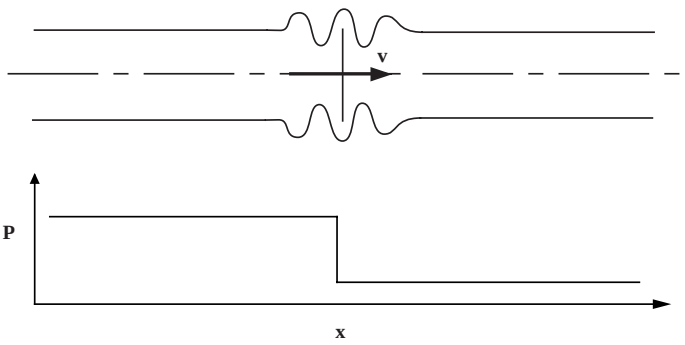

Figure 1: Schematic of configuration for excitation of shell flexural waves by shock loading.

The simplest dynamic model describes the radial (breathing) motion of the shell cross section. For uniform sudden loading, this results in a maximum strain that is twice the equivalent static loading. In order to accurately predict the response to a traveling load, one has to model the *dynamic flexural* behavior of the shell. Several models have been developed to describe this phenomenon. These models primarily differ in the manner of treating rotary inertia and transverse shear deformation. These models predict the existance of a so-called critical velocity. When the shock wave travels at the critical velocity, the resonant condition, the solution for the radial motion of the shell becomes unbounded. Evidently, damping, nonlinearities, and plastic deformation will be controlling parameters in this case. With the exception of the singular behavior at the resonant condition, the dynamic flexural model predictions are in reasonable agreement with the measured strains.

It is clear that the "critical velocity" concept should be of concern for the design of structures that are subjected to moving loads. The concept not only applies to shells with internal shock loading, but also to the structural response of gun tubes, the interaction between railroad track and soil for a moving load, and the response of structures to detonation loading. The structural response of shells to shock or detonation loading was studied by Tang (1965), Reismann (1965), de Malherbe et al. (1966) and Simkins (1987). Related research for other types of structures and loadings can be found in Felszeghy (1996a), Felszeghy (1996b), Pan et al. (1994), Dieterman and Metrikine (1997), and Dieterman and Metrikine (1996). An overview of numerical methods in the prediction of the structural response to blast and shock loading was recently presented by Mackerle (1996).

2 Analytical models

The analytical model used in this section was presented by Tang (1965). His formulation was rewritten to enable an easy comparison with the model presented by Simkins (1987).

2.1 Basic equations

The basic equations for this model are

$$\frac{\partial N_{xx}}{\partial x} = \rho h \frac{\partial^2 u}{\partial t^2} \quad ; \quad \frac{\partial M_{xx}}{\partial x} - Q_x = \rho h^3 \frac{\partial^2 \psi}{\partial t^2}$$

$$\frac{\partial Q_x}{\partial x} - \frac{N_{\theta\theta}}{R} + \Delta p = \rho h \frac{\partial^2 w}{\partial t^2}. \qquad (1)$$

The stress resultants N_{xx}, $N_{\theta\theta}$ and M_{xx} are

$$N_{xx} = \frac{Eh}{1-\nu^2}\left[\frac{\partial u}{\partial x} + \nu \frac{w}{R}\right] \quad ; \quad M_{xx} = \frac{Eh^3}{12\,(1-\nu^2)} \frac{\partial \psi}{\partial x}$$

$$N_{\theta\theta} = \frac{Eh}{1-\nu^2}\left[\nu \frac{\partial u}{\partial x} + \frac{w}{R}\right] \quad ; \quad Q_x = \kappa G h \left[\psi + \frac{\partial w}{\partial x}\right], \quad (2)$$

where κ is the shear correction factor and ψ is the rotation. The value of the shear correction factor is determined

from the condition that waves with very small wave numbers propagate at the speed of Rayleigh waves. Rotary inertia and transverse shear deformation are included in the equations. Axial prestress is neglected. For a discussion on axial prestress the reader is referred to Reismann (1965).

We introduce the following dimensionless quantitities to facilitate discussion of these equations

$$\overline{u} = \frac{u}{h} \;;\; \overline{w} = \frac{w}{h} \;;\; \overline{\psi}_x = \frac{1}{\sqrt{12}}\psi_x \;;\; \overline{\eta} = \frac{\sqrt{12}}{h}\left[x - vt\right]. \quad (3)$$

The following parameters are used in the analysis:

$$\begin{aligned}
\Lambda_j &= \frac{(p_j - p_{atm})\,R^2}{Eh^2} && \text{: excitation parameters (j} = 1, 2) \\
v_d &= \sqrt{\frac{E}{\rho\,(1-\nu^2)}} && \text{: dilatational wave velocity} \\
v_s &= \sqrt{\frac{\kappa G}{\rho}} && \text{: shear wave velocity} \\
\beta &= \frac{h}{\sqrt{12}R} && \text{: shell thickness parameter...}
\end{aligned} \quad (4)$$

The first relation in Eq. 1 is used to eliminate the axial displacement $\overline{u}$. The radial displacement $\overline{w}$ is now split up into two parts:

$$\overline{w} = \overline{w}_b + \overline{w}_s \quad ; \quad \overline{\psi}_x = -\frac{\partial \overline{w}_b}{\partial \overline{\eta}}. \quad (5)$$

Inserting these expressions into Eqs. 1 and 2, and integrating with respect to $\overline{\eta}$ gives

$$\overline{w}_s = -\left(\frac{v_d}{v_s}\right)^2 \left[1 - \left(\frac{v}{v_d}\right)^2\right] \frac{\partial^2 \overline{w}_b}{\partial \overline{\eta}^2}. \quad (6)$$

The final result for this model is the following differential equation:

$$A_4 \frac{\partial^4 \overline{w}_b}{\partial \overline{\eta}^4} + A_2 \frac{\partial^2 \overline{w}_b}{\partial \overline{\eta}^2} + A_0 \overline{w}_b = F\left(\overline{\eta}\right) \quad (7)$$

where

$$\begin{aligned}
A_4 &= \left[\left(\frac{v}{v_d}\right)^2 - 1\right]\left[\left(\frac{v}{v_s}\right)^2 - 1\right] \\
A_2 &= \left(\frac{v}{v_d}\right)^2 \left[1 + \beta^2 \left(\frac{v_d}{v_s}\right)^2\right] - \beta^2\left(1-\nu^2\right)\left(\frac{v_d}{v_s}\right)^2 \\
A_0 &= \beta^2 + \frac{\beta^2\nu^2}{\left[\left(\frac{v}{v_d}\right)^2 - 1\right]} \\
F\left(\overline{\eta}\right) &= \beta^2\left(1-\nu^2\right)\left\{\Lambda_1 + \left(\Lambda_2 - \Lambda_1\right)\left[1 - H\left(\overline{\eta}\right)\right]\right\}.
\end{aligned} \quad (8)$$

For $v_s \to \infty$ and $\left(\frac{v}{v_d}\right) \ll 1$, the model reduces to that described by Simkins (1987). In the Simkins model, the effects of transverse shear and rotary inertia are neglected.

2.2 Dispersion equation

The solution of Eq. 7 is composed of a homogeneous and inhomogeneous part. By assuming an exponential dependence, $\overline{w} \sim exp(\alpha\overline{\eta})$, for the homogeneous part, the following dispersion equation is obtained:

$$A_4\,\alpha^4 + A_2\,\alpha^2 + A_0 = 0 \quad (9)$$

where α is related to the wave number k through

$$k = \frac{\sqrt{12}\alpha}{ih}. \quad (10)$$

The characteristic roots can be determined for each value of v by simply using the quadratic formula. Based on the values of the speed v, five different cases can be distinguished. In the present investigation, only the first two cases are relevant. In the first case, $0 < v < v_{c0}$, the values of α are complex: $\alpha = \pm n \pm im$. In the second case, $v_{c0} < v < v_{c1}$, the values of α are purely imaginary: $\alpha = \pm im_1$ and $\alpha = \pm im_2$. The speed v_{c0} is the first critical velocity. The values of each critical velocity can be calculated from the vanishing of the discriminant

$$A_2^2 - 4A_0A_4 = 0. \quad (11)$$

For the Tang model, there are four critical velocities. The other critical velocities are v_{c1}: the shear wave speed v_s, v_{c2}: the dilatational wave speed in a bar $v_d\sqrt{1-\nu^2}$, and v_{c3}: the dilatational wave speed v_d. For a more detailed discussion on these five cases, the reader is referred to Tang (1965).

2.3 Case 1: $0 < v < v_{c0}$

Case 1 is referred to as the subcritical case. The axial domain is split up into two regions. Region I is after the shock, $\overline{\eta} < 0$, and region II is before the shock, $\overline{\eta} \leq 0$. In the subcritical case there are four complex roots. Continuity conditions have to be satisfied at $\overline{\eta} = 0$ for displacement, rotation, moment, and shear. The solution also must remain bounded for $\overline{\eta} \to \pm\infty$. The final solution is

$$\begin{aligned}
\overline{w}_b^I &= \Lambda_1^s - \left(\Lambda_2^s - \Lambda_1^s\right)\cdot \\
&\quad \left\{1 + \frac{1}{8}e^{n\overline{\eta}}\left[-4\cos\left(m\overline{\eta}\right) + 2\frac{n^2 - m^2}{nm}\sin\left(m\overline{\eta}\right)\right]\right\}
\end{aligned} \quad (12)$$

$$\begin{aligned}
\overline{w}_b^{II} &= \Lambda_1^s + \left(\Lambda_2^s - \Lambda_1^s\right)\cdot \\
&\quad \left\{\frac{1}{8}e^{-n\overline{\eta}}\left[4\cos\left(m\overline{\eta}\right) + 2\frac{n^2 - m^2}{nm}\sin\left(m\overline{\eta}\right)\right]\right\}
\end{aligned} \quad (13)$$

where

$$\Lambda_i^s = \frac{\beta^2\left(1-\nu^2\right)}{A_0}\Lambda_i. \tag{14}$$

The solution is oscillatory with an exponential decay as distance increases from the shock wave. Note that there are waves (precursors) ahead of the pressure front. The frequency of these precursor waves is equal to the frequency of the main signal, which exists after the shock has passed. When the velocity approaches v_{c0}, the value of n goes to zero and the solution becomes unbounded.

2.4 Case 2: $v_{c0} < v < v_{c1}$

Case 2 is referred to as the supercritical case. In the supercritical case there are only purely imaginary roots. The axial domain is also split up into two regions for this case. Continuity conditions must also be satisfied at $\overline{\eta} = 0$. However, the solution always remains bounded for $\overline{\eta} \to \pm\infty$, so other conditions have to be used to solve the problem. The extra restrictions for this case are a radiation condition; energy has to flow away from the pressure step. By using the group velocity concept, one finally has

$$\overline{w}_b^I = \Lambda_1^s + \left(\Lambda_2^s - \Lambda_1^s\right)\left\{1 + \left[\frac{m_2^2}{m_1^2 - m_2^2}\right]\cos\left(m_1\overline{\eta}\right)\right\} \tag{15}$$

$$\overline{w}_b^{II} = \Lambda_1^s + \left(\Lambda_2^s - \Lambda_1^s\right)\left[\frac{m_1^2}{m_1^2 - m_2^2}\right]\cos\left(m_2\overline{\eta}\right). \tag{16}$$

The supercritical solution is purely oscillatory. Both before and after the shock the amplitude of the signals is constant, but the frequencies are different. The precursor wave contains a higher frequency signal than the main wave. As the velocity approaches v_{c0}, m_1 approaches m_2 and the solution becomes unbounded.

3 Finite element model

The finite element calculations were carried out with the commercial package, IDEAS. In order to calculate the structural response, the problem was split up into two parts: a static calculation and a dynamic calculation. The static deformation corresponding to the pressure difference $(p_1 - p_{atm})$ was calculated with a linear-elastic static model. The dynamical response to a pressure step with amplitude $(p_2 - p_1)$ travelling at speed v was calculated with a transient, linear-elastic, finite-element model. Both results were combined to obtain the final solution.

3.1 Static calculation

The static deformation due to a pressure difference $(p_1 - p_{atm})$ was calculated. Rotary-symmetric, Mindlin-type, two-noded shell elements were used. The tube of interest was divided into 1500 elements (see section 3.2). Both ends of the tube were assumed to be fully clamped. The material and geometrical data are given in section 4.4.

3.2 Dynamic calculation

A transient, linear-elastic calculation was carried out to determine the structural response to a moving pressure step with amplitude $(p_2 - p_1)$. For the tube of interest, 1500 elements were used in the axial direction. This number was determined by accuracy and calculation time considerations. A single case was computed at a number of different resolutions using from 500 to 1500 elements. The maximum strain at several locations was plotted vs. the number of elements, and it was apparent that little gain in accuracy would result from using more than 1500 elements. For the strain signals of interest, with a speed of approximately 1000 m/s and a frequency of 35 kHz, this means a resolution of about 50 elements per wavelength. The loading of the shell is highly transient. In each node, a force was prescribed as a function of time.

The force history for each point depends on its axial location, the speed of the shock wave and the amplitude of the pressure step. The response was calculated up to the time of reflection of the shock wave at the end of the tube. For the time integration, 1000 intervals were used. For the problem of interest this means approximately 30 steps per cycle. The response was calculated with a normal mode superposition technique. The modes of vibration of the shell were calculated first. These eigenmodes were then used as a basis to calculate the transient shell response. In the calculations, 230 modes were used. The eigenfrequencies of these modes range from 3 kHz to 150 kHz.

4 Experimental setup

4.1 GALCIT 6-inch shock tube facility

The experiments were carried out with the GALCIT 6-inch shock tube. The gas in the driver and the driven sections were separated by a 0.010 inch-thick aluminum sheet. Both the driver and the driven sections of the shock tube were evacuated before each run. The driven section was then slowly filled with air until the desired pressure p_1 was reached. Next, helium was slowly released into the driver section until the diaphragm could not withstand the pressure and ruptured. The aluminum diaphragm ruptured at a pressure difference of approximately 275 kPa. Symmetric rupture of the diaphragm was ensured by the use of sharp blades placed inside the shock tube. A shock wave was then

created in the vicinity of the diaphragm and propagated toward the test section.

4.2 Tube assembly

The test section consisted of a test tube, a transition tube, and a shield tube (see Fig. 2). One end of the test tube was inserted into a hole in a flange at the end of the transition tube. The other end was connected to a 1.27 cm thick end plate. O-rings were used at both ends to make gas-tight seal connections.

The transition tube was 0.260 m long and made of 6.35 mm thick steel with an inner diameter of 50.8 mm. The transition tube had two flanges at both ends. One end of the tube was connected to the driven section of the 6-inch shock tube. The purpose of this tube was to prevent the expansion wave, generated at the area change, from entering the test tube during the duration of the test. The shield tube was made of 6.35 mm thick steel with an inner diameter of 88.9 mm. One end of the shield tube was bolted to the end plate and the other end to one of the flanges of the transition tube. The shield tube was designed to contain fragments in case of a failure of the test tube.

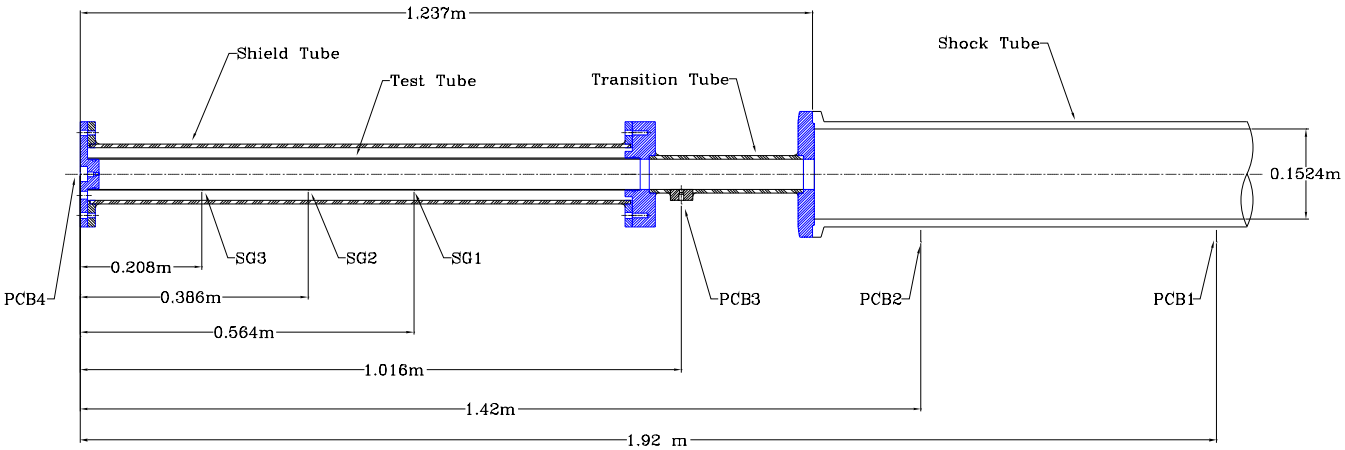

Figure 2: Tube assembly.

4.3 Instrumentation

PCB piezo-electric pressure transducers were used to determine the velocity and position of the shock wave. Two pressure transducers, 0.500 m apart, were installed near the end of the driven section of the shock tube. These transducers were used to measure the velocity in the shock tube. In addition, the output from the first transducer was used to trigger the data-acquisition system. Because the diameter of the test tube differs from the diameter of the shock tube, the shock wave travels at a different velocity inside the test tube. In order to determine the velocity of the shock wave inside the test tube, two additional pressure transducers were used. The third pressure transducer was installed near the end of the transition tube. The fourth pressure transducer was installed at the endplate, which was located 0.983 m from the third pressure transducer.

Three Micro Measurements strain gages were used to record the transient response of the test tube. The strain gages were installed 0.179 m apart, with the first strain gage located 0.382 m from the beginning of the test tube. The strain gages were mounted to measure the circumferential strain. The output from the strain gages was directed to unbalanced Wheatstone bridge circuits and amplified. The amplifiers were set at a gain of 100 and a bandwith of 100 kHz. In this way the jump in strain relative to the initial compressive strain was measured. The initial compressive strain was caused by the evacuation of the tube to the subatmospheric pressure p_1. Since the width of the strain gages is small compared to the structural wave length, the high frequency strain signals can be measured with sufficient accuracy.

4.4 Properties of the setup

The computed results are sensitive to variations in the input data. Therefore the material and geometrical properties of the tube were determined accurately. The inner diameter of the tube was measured at 8 points. The average inner diameter was 50.57 mm. The variation in inner diameter was smaller than 0.25 mm. The outer diameter of the test tube was measured at 12 equally spaced points. The average outer diameter was 53.77 mm, with a variation smaller than 0.25 mm. The total length of the tube was 0.933 m with a total mass of 0.679 kg. The effective length of the tube between the clamps is 0.889 m. The geometrical and

material data that were used in the calculations are summarized in table 1.

R:	26.09	mm	ρ:	2773	kg/m^3
h:	1.601	mm	ν:	0.33	
l:	889.0	mm	E:	$72 \cdot 10^9$	N/m^2

Table 1: Geometrical and material properties

The critical velocity, calculated from the Tang model, is 963 m/s. Neglecting rotary inertia and transverse shear, the Simkins model, gives a critical velocity of 987 m/s.

4.5 Pressure traces

The initial pressure was varied between 6.8 kPa and 18.5 kPa in order to obtain different speed shock waves. This variation in pressure was accounted for in the data reduction by scaling the measured deformations with the equivalent static value based on the pressure jump across the shock. In Fig. 3 the pressure signal of the third transducer is plotted for a shock speed of 999.2 m/s.

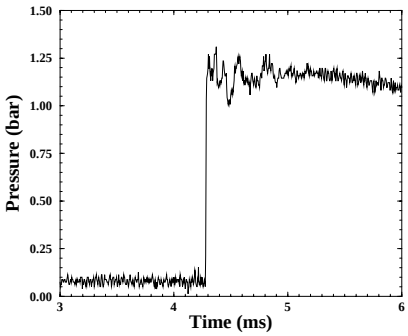

Figure 3: Pressure transducer 3 signal for $v = 999.2$ m/s.

Figure 3 shows that the pressure history is not a clearly defined step. After the shock has passed, the pressure gradually drops. Therefore it is difficult to clearly identify the post shock pressure p_2. The two PCB transducers in the driven section of the shock tube also show a slight decrease in pressure following the shock arrival. Due to the difficulty in defining the post-shock pressure, the shock wave arrival times were used to compute shock speed and then we back-calculated the pressure p_2 from the pressure p_1, the speed of the shock wave v, and the shock jump conditions.

5 Results and discussion

5.1 Strain vs. time

In Fig. 4, the jump in circumferential strain vs. time is plotted for a subcritical shock speed of 967.8 m/s. In Fig. 5 the strain is plotted for a supercritical shock speed of 999.2 m/s. In both cases the strain significantly exceeds the equivalent static strains. There are some clear differences between the subcritical and the supercritical strain traces. For the subcritical case, the strain signal is oscillatory with an exponential decay, as predicted by the analytical models and the finite element model. The period of oscillation in the precursor wave and the bulk signal is approximately the same.

In the supercritical case, the frequency in the precursor wave is higher than the frequency of the bulk signal, as predicted by the theory. However, the analytical model predicts a constant amplitude in the precursor wave, which is clearly not the case in the experimental results. This is caused by transient effects due to the finite length of the tube. Initially the whole tube is at rest. Therefore it takes time for the deflection profile to develop. The fastest waves in the shell are the dilatational waves that travel at about 5000 m/s. Before these waves arrive, the shell is at rest. The finite element model is able to account for these transient effects. The shape of the envelope of the precursor wave is also an indication whether the speed of the shock wave is subcritical or supercritical.

Another transient effect is related to the reflection of structural waves at the end of the shell. Due to the reflections at the end, there will be an interference with forward travelling waves, which can lead to high strains especially near the critical velocity, when the precursor wave is relatively strong.

5.2 Dispersion curve

The experimental and finite element data are used to reconstruct the dispersion curve for this setup. First, the lowest critical velocity is computed from the implicit solution of Eq. 11 by numerical iteration for the Tang model. The Simkins model is a special case for which an analytic solution can be found

$$v_{c0} = \sqrt{\frac{Eh}{\rho R}} \left[\frac{1}{3(1-\nu^2)} \right]^{1/4}. \qquad (17)$$

The dispersion curve is computed from Eq. 9 and the frequency is defined by Eq. 10, where the wavenumber is given by $k = 2\pi f/v$ and f is the frequency.

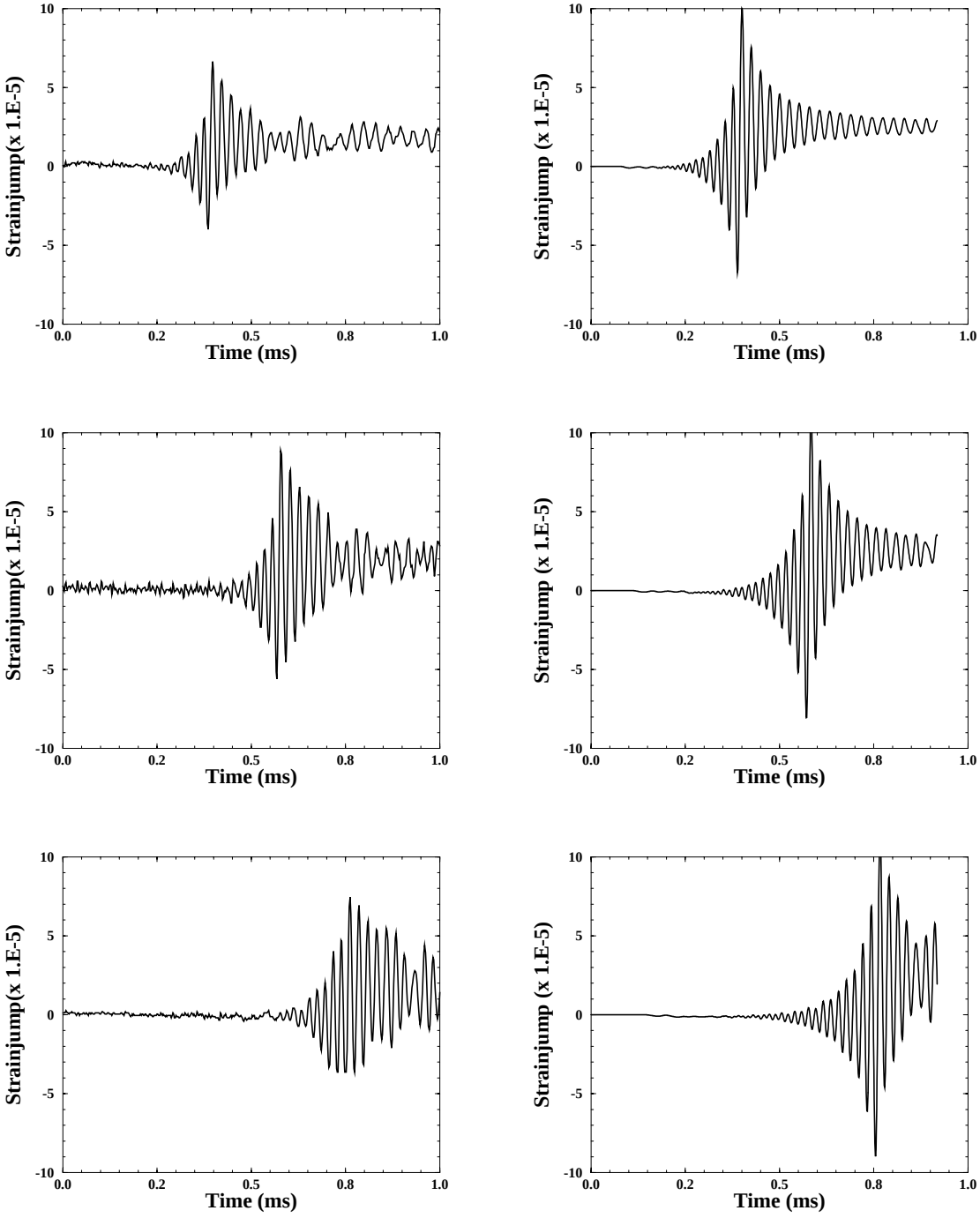

Figure 4: Strain vs. time for $v = 967.8\ m/s$. Left column: measurements. Right column: finite element results. Top: strain gage 1. Middle: strain gage 2. Bottom: strain gage 3.

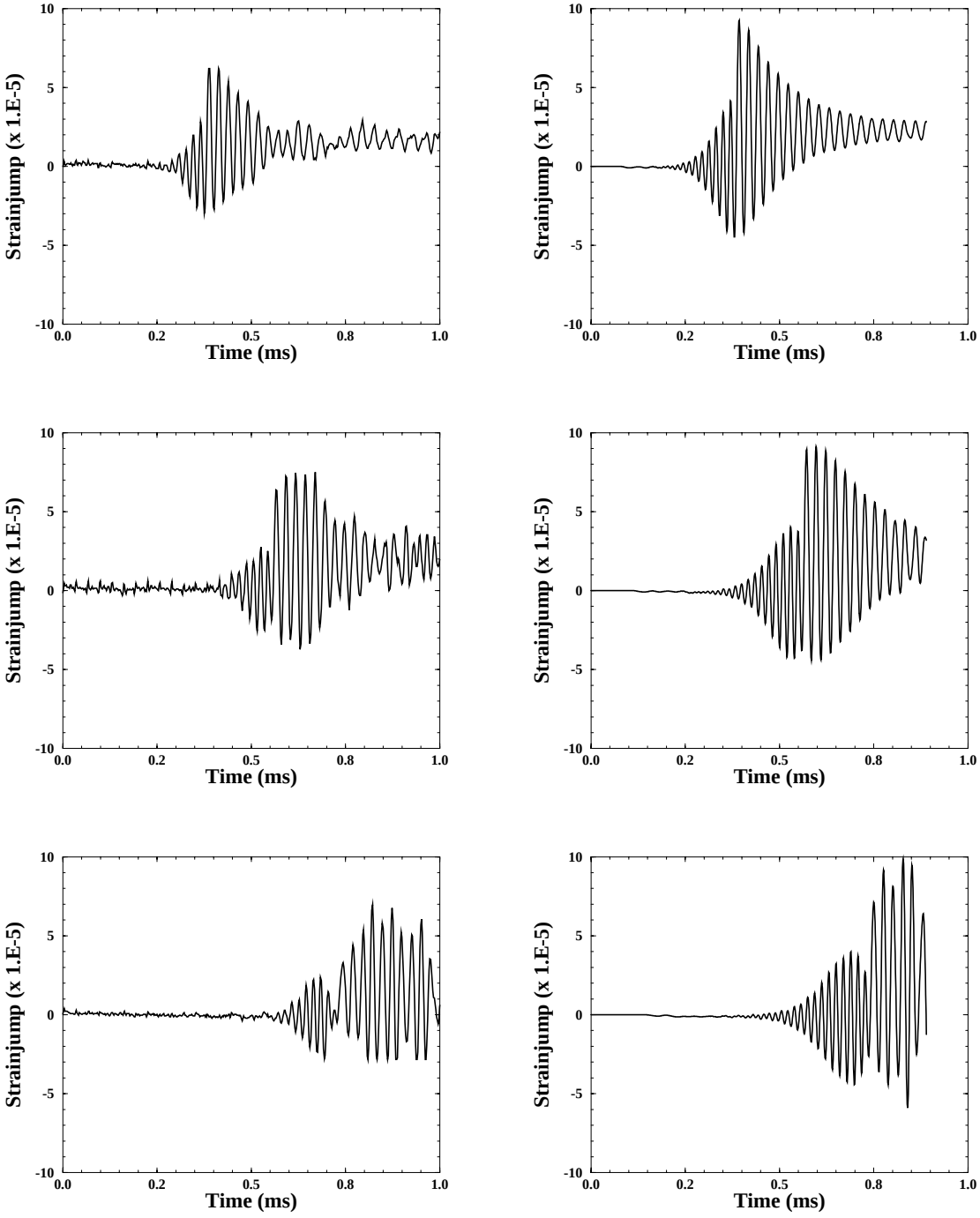

Figure 5: Strain vs. time for $v = 999.2\ m/s$. Left column: measurements. Right column: finite element results. Top: strain gage 1. Middle: strain gage 2. Bottom: strain gage 3.

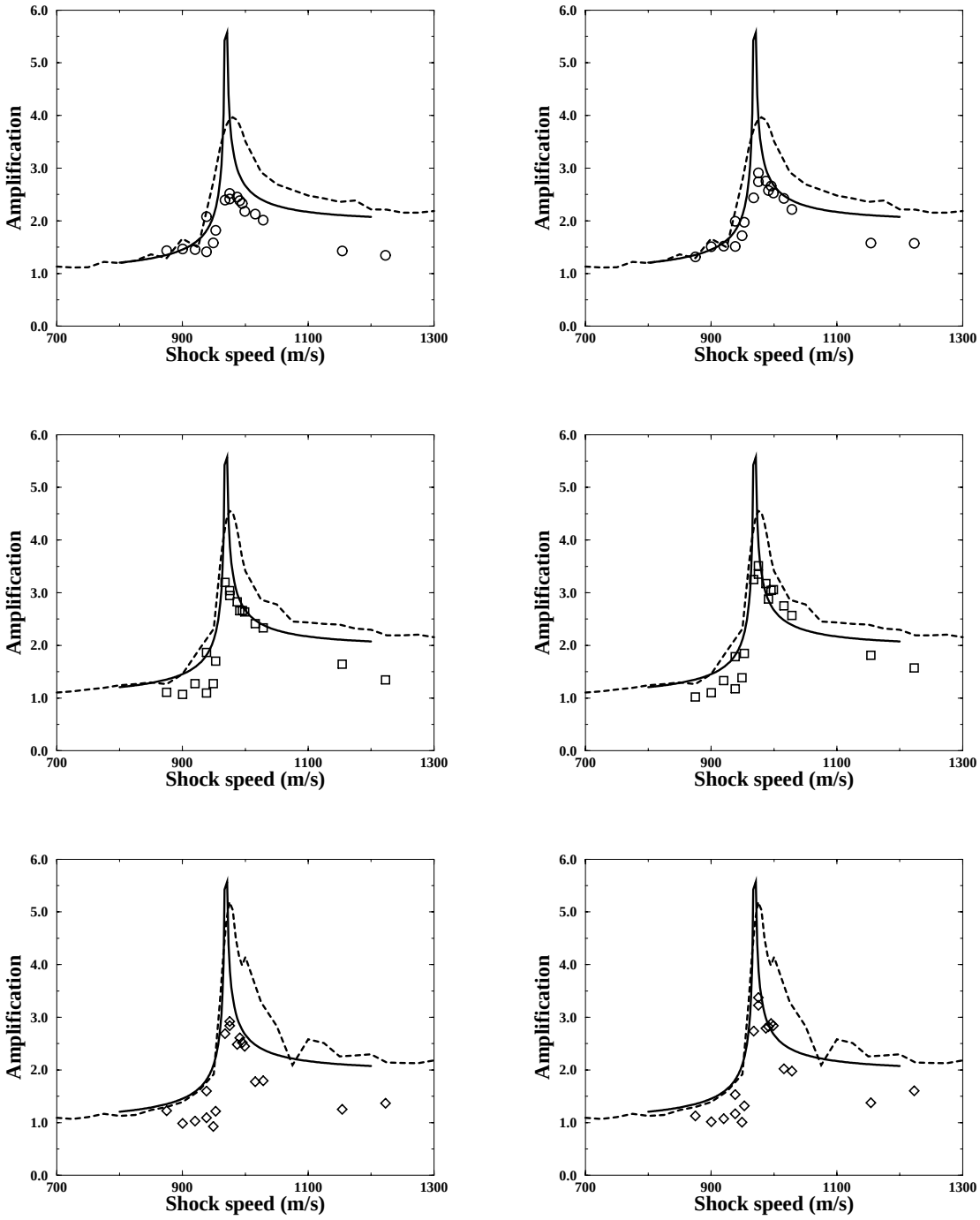

Figure 6: Amplification factor vs. velocity. Top: strain gage 1. Middle: strain gage 2. Bottom: strain gage 3. Left column: reference based on shock jump conditions. Right column: reference based on measured pressures. Solid line: Tang model. Dashed line: FEM. ○, □, ◇: Experiments.

The analytical expressions, given in Sections 2.3 and 2.4, for the strain history are used to curve fit the experimental data. The value(s) of the parameter m (subcritical case) or m_1 and m_2 (supercritical case) result from a nonlinear least-squares fitting procedure that minimized the deviations between model and experimental data over a portion of the strain history. These numbers represent the (dimensionless) frequency of oscillation. The values of these parameters are determined for each strain gage before and after the shock. For subcritical velocities, the curve fit is not very accurate. Due to the sharp exponential decay, the signal-to-noise ratio is poor and explains the large spread in results for these velocities. However, for velocities near the critical velocity or supercritical velocities, the frequency can be determined with a reasonable degree of accuracy.

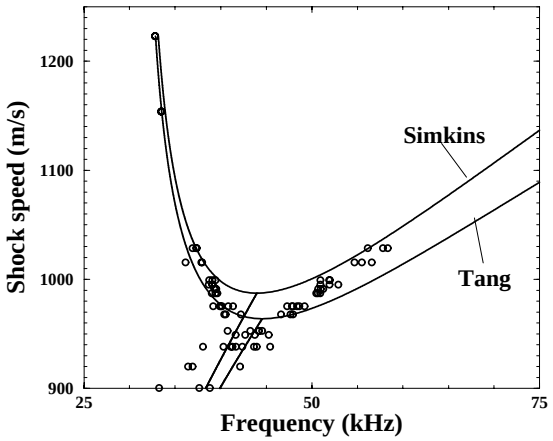

Figure 7: Dispersion curve.

The shock velocity is plotted vs. the frequency of oscillation in Fig. 7. The figure shows a clear branching of the dispersion curve as predicted by the analytical models. For supercritical velocities, the precursor wave contains the higher frequency signal (right branch), and the main wave contains the lower frequency signal (left branch). The dispersion curve offers an alternative way to extract the critical velocity from the experimental data. The branching in the experimental data occurs between 960 m/s and 970 m/s and is close to the values predicted by the analytical models. In general, the agreement between theory and experiment is reasonable.

5.3 Amplification Factor

The *dynamic amplification factor* is defined as the ratio between the maximum jump in strain from the initial state to the final state in the dynamical case and the static case. This dimensionless quantity indicates the degree of dynamic deformation; this is not affected by the initial prestress. The amplification factor is a function of shock speed v. For the analytical models presented in Section 2, the dynamic amplification factor becomes unbounded when the velocity of the shock wave is equal to the critical velocity.

The experimental and finite element results are now used to construct an amplification curve. When comparing these results to the results from the analytical models, one must be aware that certain transient phenomena are not included in the analytical models. Reflections will affect the strain history near the critical velocity, especially for the third strain gage. In the analytical models there is always a clear maximum. However, the experimental strain traces are more complicated due to the interference of the incident and reflected waves (see Fig. 4 and Fig. 5). It is therefore difficult to assign a peak value that is a consequence only of forward traveling waves, as in the analytical models. In the present investigation, the maximum jump in strain up to the time of reflection of the shock wave is used to calculate the amplification factor. This means that in some cases this value will include some contributions from reflected waves.

The calculated and measured amplification curves for the three strain gages are plotted in Fig. 6. In order to calculate the amplification factor, the maximum excursion in strain is divided by the static strain corresponding to the pressure difference $(p_2 - p_1)$. The left column of Fig. 6 is based on static strained computed from the initial pressure p_1, the shock speed v, and the shock jump conditions. The right column of Fig. 6 is based on the measured pressures. As shown, there are no visible differences between the two approaches.

The amplification curves clearly illustrate the importance of the critical velocity concept. For subcritical cases, the amplification factor is close to one, as expected for a uniform static load. For supercritical cases, the amplication factor is close to two, as expected for a suddenly-applied uniform load. The data show a maximum deflection near the critical velocity, however the measured maximum amplification factors are substantially lower than the values predicted by the finite element model. This discrepancy can partly be attributed to the fact that no damping was included in the calculations. The finite element model also predicts an increase of maximum amplification factor with distance (see Fig. 6). In the experimental results, the amplification factors for the first strain gage are lower than the following two gages, consistent with this prediction.

Summary

Calculations and experiments were carried out to study the structural response of a shell to internal shock loading. In the experiments, strains exceeding the static strain by a factor of up to 3.5 were obtained. The large strains can be explained with the critical velocity concept.

The general agreement between calculations and experiments is reasonable. The dispersion curve agrees well with the analytical predictions. The analytical models and the finite element model are able to predict the general shape of the amplification curves. However, near the critical velocity the predicted strains are too high.

Typical transient effects were observed in the experiments. These effects are related to the development of the deformation profile and the reflection of structural waves. These transient effects were taken into account in the finite element model.

This study provides a characterization only of the linear-elastic aspect of this problem. Plastic deformation and processes leading to material failure will be examined in future studies.

Acknowledgments

This research was sponsored by the Netherlands Organization for Scientific Research (NWO). Their support is gratefully acknowledged.

References

de Malherbe, M., R. Wing, A. Laderman, and A. Oppenheim, 1966. Response of a cylindrical shell to internal blast loading. *Journal of Mechanical Engineering Science*, Vol. 8(1), 91–98.

Dieterman, H. and A. Metrikine, 1996. The equivalent stiffness of a half-space interacting with a beam. critical velocities of a moving load along the beam. *European Journal of Mechanics, A/Solids*, Vol. 15(1), 67–90.

Dieterman, H. and A. Metrikine, 1997. Steady-state displacements of a beam on an elastic half-space due to a uniformly moving constant load. *European Journal of Mechanics, A/Solids*, Vol. 16(2), 295–306.

Felszeghy, S., 1996a. The Timoshenko beam on an elastic foundation and subject to a moving step load, part I: steady-state response. *Journal of Vibration and Acoustics*, Vol. 118, 277–284.

Felszeghy, S., 1996b. The Timoshenko beam on an elastic foundation and subject to a moving step load, part II: transient response. *Journal of Vibration and Acoustics*, Vol. 118, 285–291.

Mackerle, J., 1996. Structural response to impact, blast and shock loadings. A FE/BE bibliography (1993–1995). *Finite Elements in Analysis and Design*, Vol. 24, 95–110.

Pan, G., H. Okada, and S. Atluri, 1994. Nonlinear transient dynamic analysis of soil-pavement interaction under moving load: a coupled BEM-FEM approach. *Engineering Analysis with Boundary Elements*, Vol. 14, 99–112.

Reismann, H., 1965. Response of a pre-stressed cylindrical shell to moving pressure load. In S. Ostrach and R. Scanlon (Eds.), *Eighth Midwest Mechanics Conference*, pp. 349–363. Pergamon Press.

Simkins, T., 1987, July. Resonance of flexural waves in gun tubes. Technical Report ARCCB–TR–87008, US Army Armament Research, Development and Engineering Center, Watervliet, N.Y. 12189–4050.

Tang, S., 1965, October. Dynamic response of a tube under moving pressure. In *Proceedings of the American Society of Civil Engineers*, Vol.5̃, pp. 97–122. Engineering Mechanics Division.